



Unlocking CO Depletion in Protoplanetary Disks. I. The Warm Molecular Layer

Kamber R. Schwarz¹ , Edwin A. Bergin¹ , L. Ilse-dore Cleev-es², Ke Zhang¹, Karin I. Öberg² , Geoffrey A. Blake³ , and Dana Anderson³

¹ Department of Astronomy, University of Michigan, 1085 South University Avenue, Ann Arbor, MI 48109, USA; kamberr@umich.edu

² Harvard-Smithsonian Center for Astrophysics, 60 Garden Street, Cambridge, MA 02138, USA

³ Division of Geological and Planetary Sciences, MC 150-21, California Institute of Technology, 1200 E California Boulevard, Pasadena, CA 91125, USA

Received 2017 November 8; revised 2018 January 29; accepted 2018 February 6; published 2018 March 27

Abstract

CO is commonly used as a tracer of the total gas mass in both the interstellar medium and in protoplanetary disks. Recently, there has been much debate about the utility of CO as a mass tracer in disks. Observations of CO in protoplanetary disks reveal a range of CO abundances, with measurements of low CO to dust mass ratios in numerous systems. One possibility is that carbon is removed from CO via chemistry. However, the full range of physical conditions conducive to this chemical reprocessing is not well understood. We perform a systematic survey of the time dependent chemistry in protoplanetary disks for 198 models with a range of physical conditions. We vary dust grain size distribution, temperature, cosmic-ray and X-ray ionization rates, disk mass, and initial water abundance, detailing what physical conditions are necessary to activate the various CO depletion mechanisms in the warm molecular layer. We focus our analysis on the warm molecular layer in two regions: the outer disk (100 au) well outside the CO snowline and the inner disk (19 au) just inside the midplane CO snowline. After 1 Myr, we find that the majority of models have a CO abundance relative to H₂ less than 10⁻⁴ in the outer disk, while an abundance less than 10⁻⁵ requires the presence of cosmic-rays. Inside the CO snowline, significant depletion of CO only occurs in models with a high cosmic-ray rate. If cosmic-rays are not present in young disks, it is difficult to chemically remove carbon from CO. Additionally, removing water prior to CO depletion impedes the chemical processing of CO. Chemical processing alone cannot explain current observations of low CO abundances. Other mechanisms must also be involved.

Key words: astrochemistry – circumstellar matter – ISM: abundances – molecular data – protoplanetary disks

Supporting material: machine-readable tables

1. Introduction

CO is arguably the mostly commonly observed molecule in astronomy, being both highly abundant and highly emissive. In molecular clouds, it is used as a tracer of the total gas mass, with an observed abundance relative to H₂ of $\sim 0.5\text{--}3 \times 10^{-4}$ (Bergin & Williams 2017). This abundance ratio is often assumed to hold for protoplanetary disks. However, as early as the first detection of CO in a protoplanetary disk, there has been a discrepancy between the gas mass inferred from CO and that estimated from the dust (Dutrey et al. 1994). Recent surveys of protoplanetary disks with ALMA have revealed that many systems have a low CO to dust mass ratio compared to the ISM (e.g., Ansdell et al. 2016; Long et al. 2017). This has been attributed to either a low total gas mass or a low abundance of CO relative to H₂ (Williams & Best 2014; Miotello et al. 2017). Distinguishing between the two scenarios requires an alternative tracer of the total gas mass, such as HD, which has been detected in three systems so far (Bergin et al. 2013; McClure et al. 2016). For all three systems, CO is underabundant, with abundances relative to H₂ in the range 10⁻⁶–2 × 10⁻⁵ (Favre et al. 2013; McClure et al. 2016; Schwarz et al. 2016). High spatial resolution observations of CO isotopes in TW Hya reveal that CO is also underabundant interior to the midplane CO snowline (Zhang et al. 2017). In this source, simple freeze out of CO onto grains is insufficient to explain the observations. Furthermore, CO is not the only underabundant volatile. TW Hya is underabundant in gas phase atomic carbon (Kama et al. 2016) and H₂O vapor is depleted in numerous systems, including TW Hya (Du et al. 2015, 2017).

Previous modeling has explored the affects of photodissociation, freeze out onto dust grains, and isotope selective self-shielding on the observed CO abundances. Williams & Best (2014) apply models that correct for a reduction in gas phase CO due to both photodissociation and freeze out to observations of disks in Taurus. Even when accounting for these effects, they find CO to dust ratios well below those measured in the ISM. CO abundance measurements are often based on observations of optically thin emission from less abundant isotopologues, using isotopologue abundance ratios to convert to a total CO abundance. Miotello et al. (2014) demonstrate that changes in isotopologue abundance ratios due to self-shielding can lead to underestimates of the CO abundance by up to an order of magnitude, but cannot explain the CO abundances in the most depleted systems. Furthermore, the CO abundances relative to H₂ based on detections of HD exclude any gas below 20 K. This is because CO freezes onto dust grains at temperatures below 20 K, while the emissivity of the HD 1-0 drops sharply for temperatures less than 20 K (Favre et al. 2013). Taken together, these studies show that, even in the warm molecular layer, CO is underabundant.

Several mechanisms have been put forth to explain the observed low CO abundances, including gas disk dispersal (Bai 2016), dust dynamics, grain growth, settling, dust drift (Salyk et al. 2008; Krijt & Ciesla 2016; Xu et al. 2017), and chemical reprocessing. Multiple studies have shown that CO can be depleted via chemical pathways within the disk (Bergin et al. 2014; Reboussin et al. 2015; Eistrup et al. 2016; Yu et al. 2016). However, to date, these studies have been limited in their scope, lacking a holistic view of the disk conditions for

which different chemical pathways are active as well as how the efficiency of such pathways vary from disk to disk. In particular, it is unclear if such mechanisms are efficient enough to fully explain the observed CO abundances without invoking other mechanisms such as grain growth.

Most chemical models require a source of ionization, with the carbon eventually converted to CO₂ ice, though other pathways have been identified. In the chemical models of Bergin et al. (2014), with physical parameters based on TW Hya, CO gas reacting with He⁺ results in much of the carbon being reprocessed into hydrocarbons, a mechanism first put forth by Aikawa & Herbst (1999). These hydrocarbons then freeze onto grains. Reboussin et al. (2015) explored a grid of chemical models spanning a range of disk temperatures and initial chemical abundances. In their models, CO is depleted by an order of magnitude for temperatures of less than 30 K, going primarily into CO₂ ice. In these models, the reprocessing of CO ice is the result of cosmic-ray induced UV photons. As such, the final ice composition depends on the incident cosmic-ray rate assumed. Eistrup et al. (2016) focus on the midplane chemistry inside of 30 au for a single disk physical model. They find that much of the CO in this region is converted to CO₂ ice, though at 30 au, a significant fraction of the carbon is found in CH₄ ice as well. Yu et al. (2016) explore the chemical effects in a warmer disk, heated by both stellar radiation and viscous heating, with an enhanced gas-to-dust ratio of 1000 compared to the commonly assumed value of 100. In their model disk, the midplane temperature is greater than the CO freeze out temperature interior to 70 au. However, CO is still depleted in the presence of cosmic-rays, with the carbon found in CO₂ ice as well as ices composed of complex organics.

Clearly, it is possible to chemically deplete CO in protoplanetary disks under a variety of physical conditions. The depletion mechanisms identified in previous work require the presence of ionizing radiation, primarily cosmic-rays, and/or warm disk temperatures, which keep CO in the gas phase. However, none of the previous studies systematically explore how different dust populations impact the chemistry. Furthermore, there is doubt as to whether high ionization rates are present in protoplanetary disks. In our own solar system, the solar wind modulates cosmic-rays within the heliosphere (Gleeson & Axford 1968). Similarly, Cleeves et al. (2013) argue that winds from T-Tauri stars can modulate the incident cosmic-ray rate for the surrounding disk. Indeed, the N₂H⁺ emission observed in TW Hya is consistent with a low cosmic-ray ionization rate (Cleeves et al. 2014). Given the expected ubiquity of stellar winds, sub-ISM cosmic-ray levels should be the norm among protoplanetary disks, removing the most commonly invoked mechanism for CO depletion.

In this paper, we aim to systematically constrain the subset of physical conditions necessary to enable chemical reprocessing of CO. To this end, we explore the chemical evolution for a large grid of physical models, varying the cosmic-ray ionization rate, the incident X-ray flux, the mass of the disk, the temperature of the disk, the fraction of dust mass in large grains. All of these parameters affect either the ionization or temperature structure. Additionally, we vary the amount of water initially available to the chemical network in order to explore how oxygen depletion impacts the carbon chemistry. Current observations of low volatile abundances primarily probe the warm molecular layer, where volatile elements such as carbon are primarily in gas phase molecules (Aikawa &

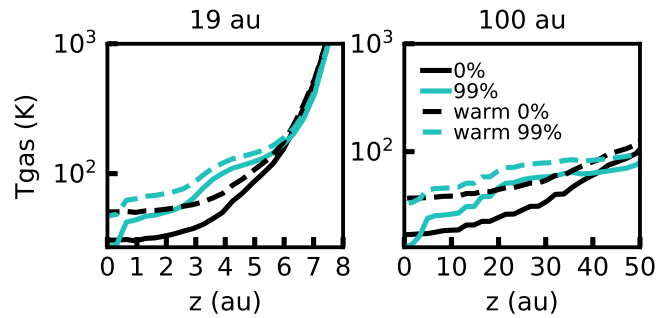


Figure 1. Vertical gas temperature profiles at 19 and 100 au for the 0.03 M_{\odot} disk. The 0% large grain model is shown in black and the 99% large grain model is shown in teal. Dashed lines indicate the temperature in the warm disk models.

Herbst 1999). In this paper, we focus on the conditions and timescales needed to chemically remove CO from the warm molecular layer. Future work will explore the results for the midplane and the implications for planet formation. Section 2 details our modeling framework and describes the parameter space covered by our grid of models. The results of our model grid are explored in Section 3. In Section 4, we compare our results to previous work and discuss the implications for observations of volatile carbon in protoplanetary disks. Finally, we summarize our findings in Section 5.

2. Model

The physical model is a two-dimensional, azimuthally symmetric disk generated using the radiative transfer code TORUS (Harries 2000), which calculates the temperature structure for a given distribution of gas and dust (Figure 1, see also Figures 12 and 13). We consider disk masses of 0.1, 0.03, and 0.003 M_{\odot} with an inner radius of 0.1 au and an outer radius of 200 au. The surface density distribution for the gas and the small grains ($r_d = 0.005\text{--}1 \mu\text{m}$) is

$$\Sigma_g(R) = \Sigma_c \left(\frac{R}{R_c} \right)^{-\gamma} \exp \left[- \left(\frac{R}{R_c} \right)^{2-\gamma} \right], \quad (1)$$

where Σ_c is the disk surface density at $R_c = 100$ au and $\gamma = 1$. The density distribution for the small grains is

$$\rho_s = \frac{(1-f)\Sigma}{\sqrt{2\pi}Rh} \exp \left[- \frac{1}{2} \left(\frac{Z}{H} \right)^2 \right]. \quad (2)$$

For the large grains ($r_d = 0.005\text{--}1000 \mu\text{m}$):

$$\rho_l = \frac{f\Sigma}{\sqrt{2\pi}R\chi h} \exp \left[- \frac{1}{2} \left(\frac{Z}{\chi H} \right)^2 \right], \quad (3)$$

where f is the fraction of the dust mass in large grains, Z is the height in the disk, and χ is the fractional scale height of the large grains. The scale height for the gas and small grains is

$$h(r) = 12 \text{ au} \left(\frac{R}{R_c} \right)^{0.3} \quad (4)$$

and

$$H = hR. \quad (5)$$

Both the small and large grains follow an MRN size distribution (Mathis et al. 1977), where $n_g \propto r_d^{-3.5}$ and have

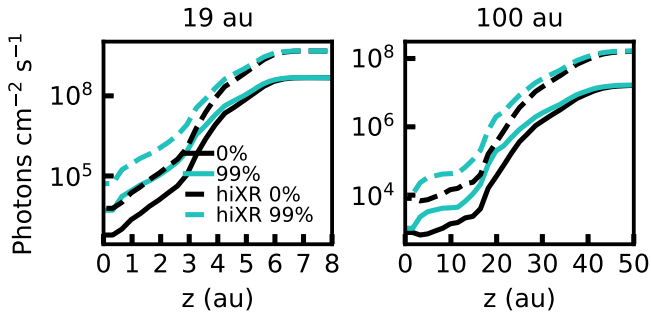


Figure 2. Vertical profiles of the integrated X-ray flux at 19 and 100 au for the $0.03 M_{\odot}$ disk. The 0% large grain model is shown in black and the 99% large grain model is shown in teal. Dashed lines indicate the temperature in the warm disk models.

optical properties consistent with a population that is comprised entirely of astronomical silicates (Draine & Lee 1984). The overall gas-to-dust mass ratio at each radius is 100. The large grains are more settled than the small grains, simulating the observed segregation between large and small grains. Balancing diffusion and settling, the fractional scale height of the large grains is

$$\chi = \sqrt{\frac{\alpha}{\alpha + \Omega t_{\text{stop}}} \frac{1 + \Omega t_{\text{stop}}}{1 + 2\Omega t_{\text{stop}}}} \quad (6)$$

(Youdin & Lithwick 2007), where $\alpha = 10^{-3}$ and Ω is the orbital frequency. Following the approach of Krijt & Ciesla (2016), we calculate the stopping time, the time required for the velocity of a grain to be reduced by a factor of e , to be

$$t_{\text{stop}} = \sqrt{\frac{\pi}{8}} \frac{\rho_g r_d}{\rho_l c}, \quad (7)$$

where $r_d = 1$ mm is the dust grain radius, ρ_g is the internal density of a grain, ρ_l is the density of large grains, and c is the speed of sound.

UV and X-ray radiative transport are computed using Monte Carlo methods as described by Bethell & Bergin (2011a, 2011b). We consider an X-ray spectrum in the range 1–10 keV. The overall integrated X-ray luminosity is either 10^{30} erg s^{-1} or 10^{31} erg s^{-1} , see Figures 2, 14, and 15 (Cleeves et al. 2015). In comparison, the X-ray luminosity of TW Hya is 2×10^{30} erg s^{-1} (Kastner et al. 1999; Raassen 2009; Brickhouse et al. 2010). We consider UV flux from the central star in the range 930–2000 Å, and include scattering of Ly α photons by hydrogen atoms as well as dust grains, see Figures 3, 16, and 17 (Bethell & Bergin 2011b). The central star is a T-Tauri star based on the properties of TW Hya. The cosmic-ray ionization rates, ζ_{CR} , and the method for calculating the attenuation are taken from Cleeves et al. (2013). We consider ζ_{CR} appropriate for the diffuse ISM (2×10^{-17} s $^{-1}$, Webber 1998) and a reduced rate consistent with the current flux in the solar system at 1 au during solar maximum (1.6×10^{-19} s $^{-1}$), the later of which results in the best agreement with the observed molecular emission from TW Hya (Cleeves et al. 2014).

Table 1 lists the set of physical conditions covered by our models. For each disk mass, we generate a model for a range of large grain fractions, f , from 0 to 0.99. Our fiducial model uses an X-ray luminosity of 10^{30} erg s^{-1} and a cosmic-ray ionization rate of 1.6×10^{-19} s $^{-1}$. The high X-ray luminosity models use an X-ray luminosity of 10^{31} erg s^{-1} with all other

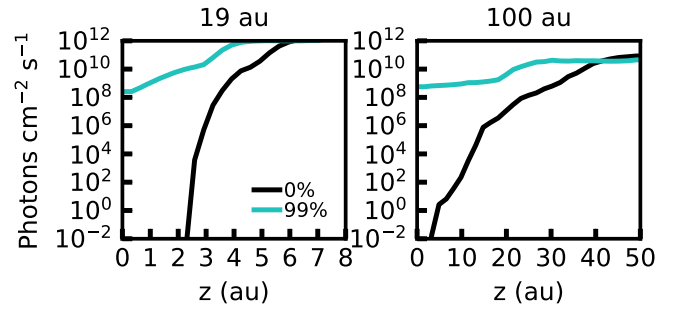


Figure 3. Vertical profiles of the integrated UV flux at 19 and 100 au for the $0.03 M_{\odot}$ disk. The 0% large grain model is shown in black and the 99% large grain model is shown in teal. Dashed lines indicate the temperature in the warm disk models.

Table 1
Physical Model Properties

Parameter	Values
$M_{\text{disk}} (M_{\odot})$	0.1, 0.03, 0.003
$L_{\text{XR}} (\text{erg s}^{-1})$	1E30, 1E31
$\zeta_{\text{CR}} (\text{s}^{-1})$	1.6E-19, 2E-17
f_l	0.0, 0.1, 0.2, 0.3, 0.4, 0.5, 0.6, 0.7, 0.8, 0.9, 0.99
$R_{\text{in}} (\text{au})$	0.1
$R_{\text{out}} (\text{au})$	200

Table 2
Initial Abundances Relative to H $_2$

Species	Abundance	Species	Abundance	Species	Abundance
H $_2$	1.00E00	NH $_3$	1.60E-07	SO	1.00E-08
He	2.80E-01	CN	1.20E-07	CS	8.00E-09
CO	2.00E-04	HCN	4.00E-08	C $^+$	2.00E-09
H $_2$ O(gr)	5.00E-04	H $_3^+$	2.00E-08	Si $^+$	2.00E-11
N	4.50E-05	HCO $^+$	1.80E-08	S $^+$	2.00E-11
N $_2$	2.00E-06	C $_2$ H	1.60E-08	Mg $^+$	2.00E-11
C	1.40E-06	H $_2$ CO	1.60E-08	Fe $^+$	2.00E-11

parameters the same as for the fiducial models, while the high cosmic-ray rate models assume $\zeta_{\text{CR}} = 2 \times 10^{-17}$ s $^{-1}$. Additionally, we consider warm disk models, in which the gas and dust temperatures have been increased by 20 K everywhere in the disk, for the fiducial and high cosmic-ray models.

Our chemical model is that described by Cleeves et al. (2014), based on the chemical networks of Fogel et al. (2011) and Smith et al. (2004) and updated to include the reaction rates from McElroy et al. (2013). The reaction network includes photodesorption, photodissociation, freeze out onto grains, cosmic-ray and X-ray ionization, gas phase ion and electron reactions, and self-shielding of H $_2$ and CO. The model also includes a limited network of grain surface reactions.

When calculating the chemistry, each radius is broken into 45 vertical zones. The chemistry in each zone is calculated independently, with the exception of self-shielding, which considers the abundances above the current zone. The dust size distribution in each zone factors into calculating the rates for reactions such as freeze out and photodesorption, where the grain surface area is important. Each zone starts with the same initial abundances relative to H $_2$, based on the abundances for the model molecular cloud of Aikawa & Herbst (1999; see our Table 2). Additionally, for the $0.03 M_{\odot}$ fiducial, high X-ray, and high cosmic-ray models, we calculate the chemistry for a reduced

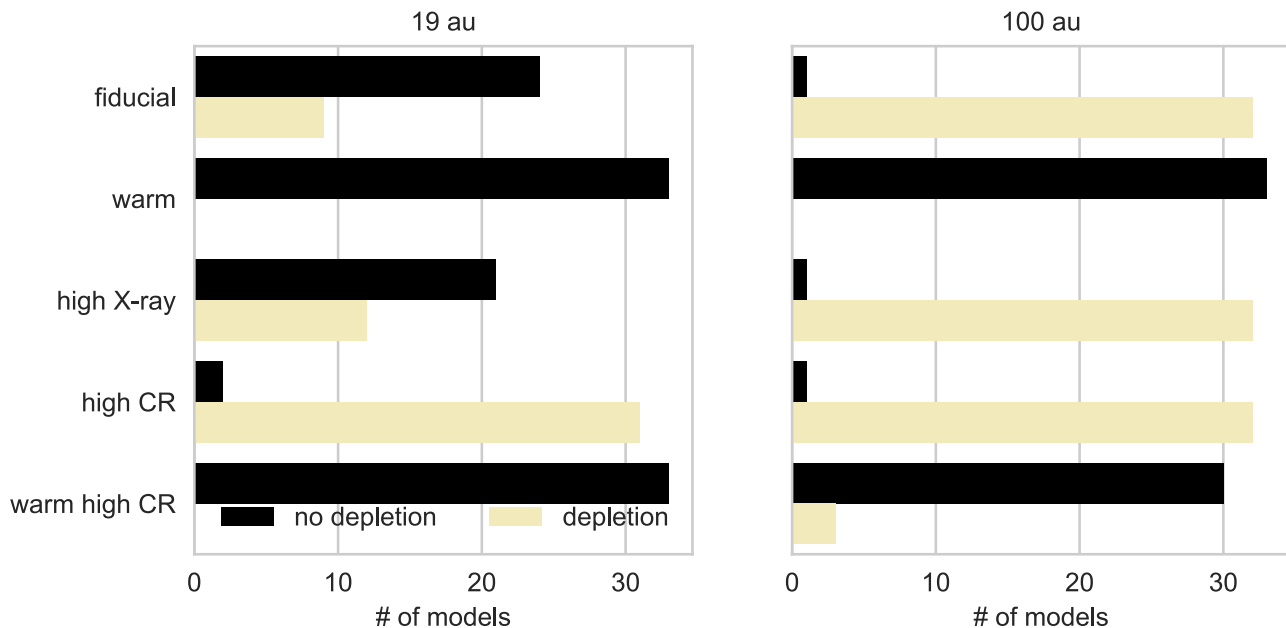


Figure 4. Breakdown of the number of models that are depleted ($N(\text{CO}) < 10^{-4}$) and not depleted ($N(\text{CO}) > 10^{-4}$) at 1 Myr.

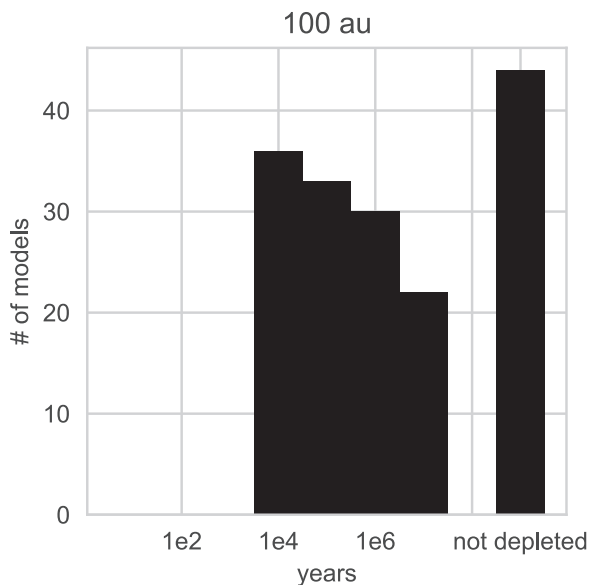


Figure 5. Time at which the CO abundance first drops below 10^{-4} at 100 au for each model.

Table 3
General CO Abundance Trends

Model Type	19 au		100 au	
	Depletion	No Depletion	Depletion	No Depletion
High CR	✓		✓	
Warm high CR		✓		✓
High X-rays		✓	✓	
Fiducial		✓	✓	
Warm fiducial		✓		✓
99% large grains	✓			✓

oxygen abundance by setting the initial H_2O ice abundance to zero. Including these models, the total number of unique models is 198. For each model, the chemistry runs for 6 Myr.

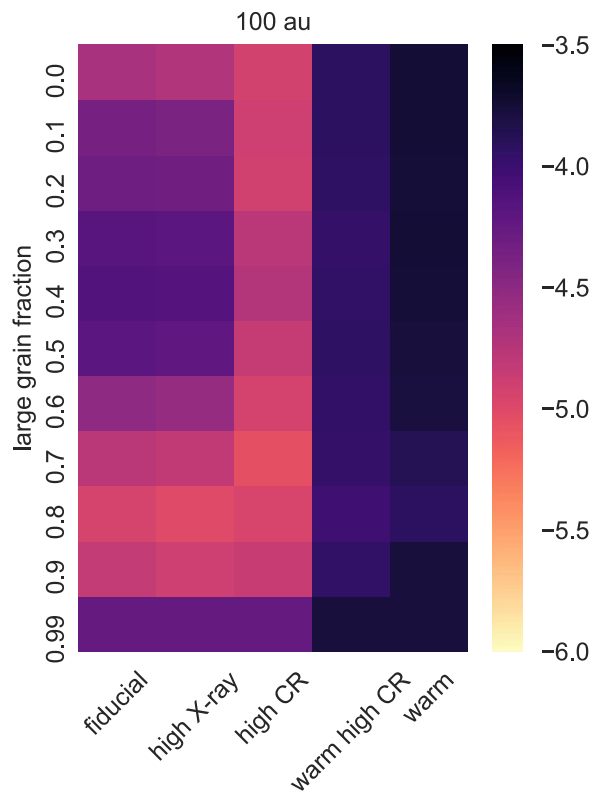


Figure 6. Log CO abundance relative to H_2 at 100 au for each model with a disk mass of $0.03 M_\odot$. Additional figures for the 0.1 and $0.003 M_\odot$ disks can be found in Appendix A.

3. Results

We focus our analysis on two radii: 19 au, which is interior to the midplane CO snowline; here defined as the location in the midplane where the CO gas and CO ice abundances are equal, and 100 au, which is typical of the outer disk. In this paper, we further focus on the vertical region known as the warm molecular layer (Aikawa & Herbst 1999), the disk region typically probed

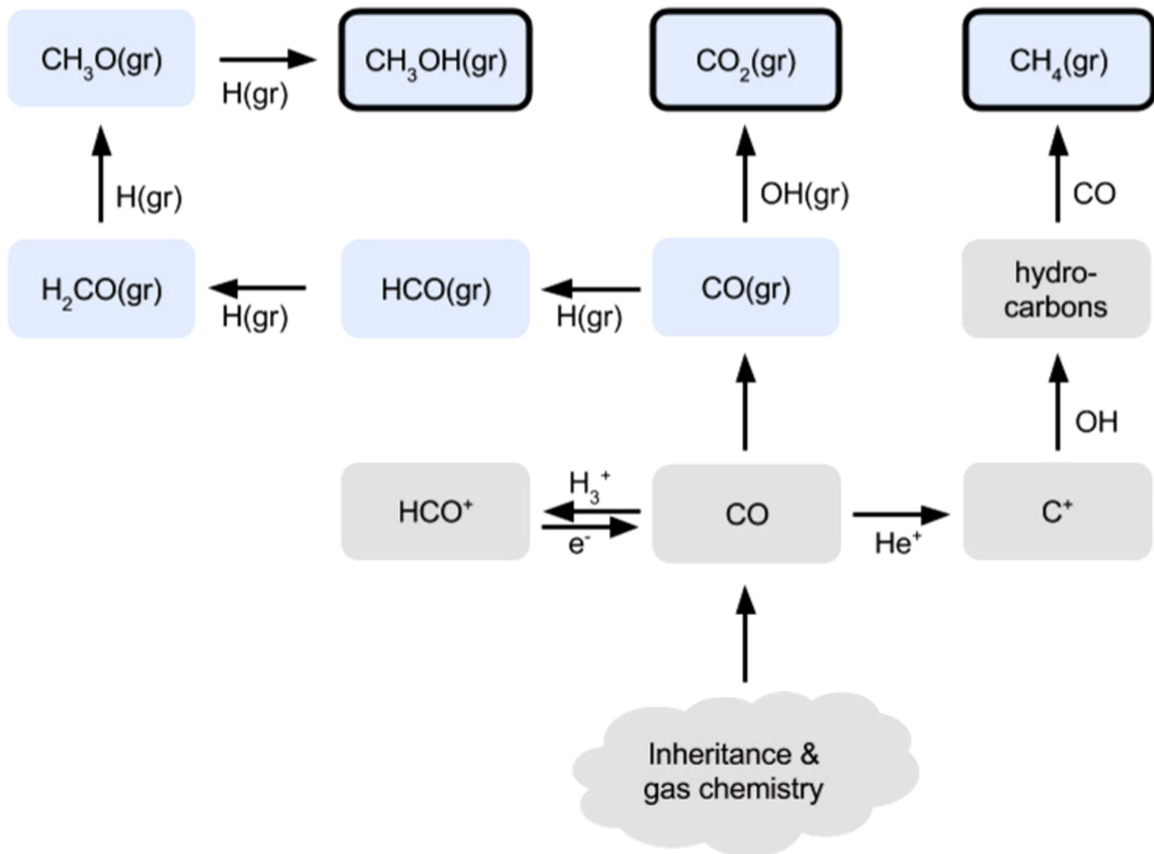


Figure 7. Schematic of the chemical reactions relevant for CO reprocessing. Gas phase species are shown in gray. Ices are shown in blue. End state species are bolded.

by observations. For the purpose of our analysis, we define the warm molecular layer as the vertical region bounded by the vertical CO snowline and the height at which the CO gas phase abundance relative to H_2 drops by a factor of $1/e$ from its peak abundance at that radius, see Figure 18 for an example. The abundances reported in this paper are calculated by vertically integrating the absolute abundance of a given species in the warm molecular layer, then dividing the resulting column density by the H_2 column density over the same region.

We run a total of 165 models with our standard, ISM initial abundance. Figure 4 and Table 3 summarize which models are able to chemically reprocess CO. Of these, in the warm molecular layer at 100 au, by 1 Myr 58.18% of models show some depletion, with CO abundances between 10^{-4} and 10^{-5} , while 1.82% of models are extremely depleted, with abundances of less than 10^{-5} . By 6 Myr, 57.58% are depleted and an additional 17.56% of models are extremely depleted. In the inner disk at 1 Myr, 18.79% of models are depleted and 12.73% are extremely depleted. By 6 Myr, 26.06% of models are depleted and 27.27% are extremely depleted. In the outer disk, most models are able to reduce the CO column density by an order of magnitude, while inside the midplane snowline a high cosmic-ray rate is generally required to remove carbon from CO. Below we discuss the conditions necessary for CO depletion in greater detail.

3.1. Outer Disk

In the warm molecular layer at 100 au, 41.8% of our 165 models have a CO abundance of less than 10^{-4} by 0.1 Myr (Figure 5), including the majority of the fiducial models, high

cosmic-ray rate models (hiCR), and high X-ray luminosity models (hiXR). Additionally, the models with high cosmic-ray rates, where the temperature has been increased by 20 K (warm hiCR), are able to deplete CO on timescales of a few million years, such that 60.0% of the models are depleted by 1 Myr, increasing to 72.1% by 3 Myr. The CO abundance in each model at 1 Myr is given in Figure 6 and Figure 20.

Figure 7 provides a schematic of the most important chemical pathways via which CO is reprocessed. In the warm molecular layer, UV photons are able to remove H_2O ice from the grain surface, creating gas phase OH and H. Both species are able to freeze out onto the grain surface. Once there, they react with CO before thermal desorption can return CO to the gas phase. This slowly builds reservoirs of CO_2 ice and, to a lesser extent, CH_3OH ice, which are able to remain on the grain surface at temperatures where CO is primarily in the gas phase (Figure 21). This reprocessing does not occur for the warm models where the temperature has been increased by 20 K (warm and warm hiCR). In these warm models, the temperature is high enough that even the less volatile species such as CO_2 cannot remain on the grain surface. Additionally, there is less CO reprocessing in models with more large grains. Large grains settle to the midplane, resulting in higher temperatures in the warm molecular layer as well as a higher flux of X-rays and UV photons (Figures 1–2), all of which aid in keeping carbon in gas phase CO.

When a high cosmic-ray rate is present, there is additional CO depletion on timescales of a few million years. A high cosmic-ray rate allows CO reprocessing to occur deeper in the disk due to the enhanced abundance of He^+ and H_3^+ . He^+ dissociates CO, leading to a series of gas phase reactions that form hydrocarbons, primarily CH_4 (Figure 7). However, it is the reaction with H_3^+ that

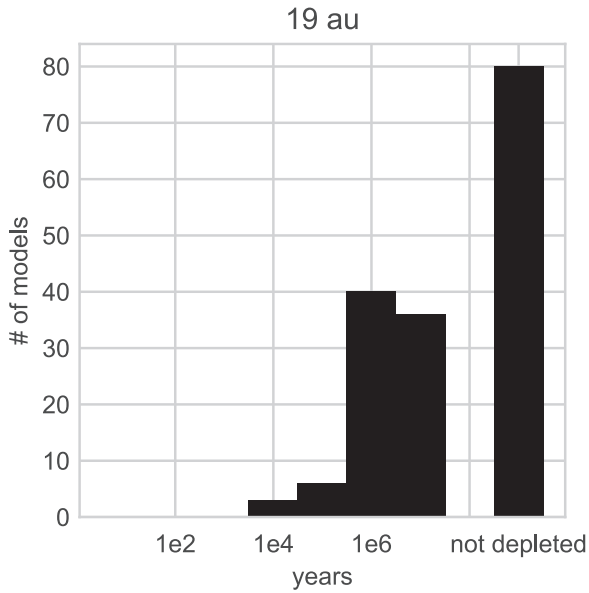


Figure 8. Time at which the CO abundance first drops below 10^{-4} at 19 au for each model.

ultimately plays a larger role in the reprocessing of CO. CO and H_3^+ react to form HCO^+ , which quickly reacts with an electron, returning the carbon to CO, while also producing atomic hydrogen (Figure 7). Some of these H atoms freeze onto the grain surface, hydrogenating CO ice and eventually forming CH_3OH ice. Because of this process, the warm hiCR models show roughly an order of magnitude of CO depletion by 3 Myr (Figure 19). CH_3OH , which has a higher binding energy than CO_2 , is able to remain frozen out even at the higher temperatures in the warm CR models. Because CH_3OH ice formation is less efficient than CO_2 ice formation, CO depletion takes longer in the warm hiCR models.

3.2. Inner Disk

At 19 au, interior to the midplane CO snowline, depletion timescales are longer with only 5.5% of models depleted after 0.1 Myr, 29.7% depleted after 1 Myr, and 48.5% depleted after 3 Myr (Figure 8). The majority of models are not depleted in CO (Figure 9). However, all of the hiCR models show CO depletion due to the increased abundance of H_3^+ . Successive hydrogenation of CO ice reduces the CO column density by more than an order of magnitude within 1 Myr for the 0.1 and $0.03 M_\odot$ disks. As the fractional dust mass in large grains increases, the disk becomes more settled, increasing the flux of UV photons in the warm molecular layer. This results in increased photodesorption of H_2O ice. As more oxygen becomes available to the chemistry H preferentially hydrogenates oxygen over CO. Ion induced CO depletion is also seen in the high X-ray luminosity models (hiXR) for the $0.003 M_\odot$ disk (Figure 22), in which the lower density allows the X-rays to penetrate deeper in the disk, producing H_3^+ , though on longer timescales than those in the hiCR models (Figure 22).

The 0.1 and $0.03 M_\odot$ fiducial and hiXR models with 99% of the dust mass in large grains are also able to chemically reprocess some CO due to the photodesorption of H_2O ice (Figures 9 and 23). The resulting OH reacts with CO ice to form CO_2 ice. At 19 au, the $0.003 M_\odot$ disk is exposed to a substantially higher flux of UV photons than either the 0.1 or $0.03 M_\odot$ disk (Figure 16). Thus, the production of CH_3OH in

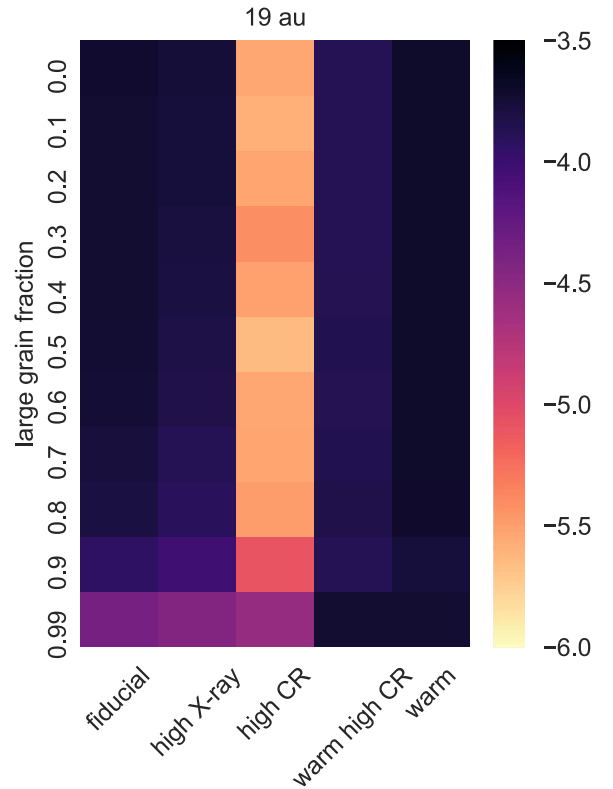


Figure 9. Log CO abundance relative to H_2 at 19 au for each model with a disk mass of $0.03 M_\odot$. Additional figures for the 0.1 and $0.003 M_\odot$ disks can be found in Appendix A.

the hiCR models is hampered by the photodesorption of H_2O , regardless of the large grain fraction. When $\sim 60\%$ of the dust mass is in large grains, the $0.003 M_\odot$ fiducial model shows some depletion of CO due to the photodesorption of H_2O ice (Figure 23). However, as the dust mass in large grains increases and the disk becomes more settled, the increased photodesorption of CO_2 and CH_3OH makes it difficult for these species to remain on the grain and carbon is instead found primarily in gas phase CO regardless of the ionization structure (Figure 25).

3.3. Dominant Carbon Carriers

The top five most abundant carbon bearing species after 1 Myr in each model are listed in Tables 4 and 5. For all models depleted in CO, carbon has become incorporated into less volatile species on the grain surface. Generally, CO_2 ice is the dominant carbon species, followed by CH_3OH ice. CO_2 can form directly from CO ice, while CH_3OH ice is formed via a series of hydrogenation reactions (Figure 7). Thus, the timescales needed to build a reservoir of CH_3OH ice are longer than those needed for CO_2 . The atomic hydrogen needed to hydrogenate CO is an end product of H_2 ionization. As such, CH_3OH can only be the dominant carbon carrier in models with a high cosmic-ray rate (hiCR or warm hiCR).

It is important to note that both CO_2 ice and CH_3OH ice are end state species in our chemical network, meaning that the sequence of grain surface reactions, which build progressively more complex species do not proceed past these two species. The absolute abundances of these ices in our models should not be taken as the expected CO_2 and CH_3OH ice abundances in observed systems. Rather, these ice abundances represent the total amount of carbon we expect to be locked up in ices.

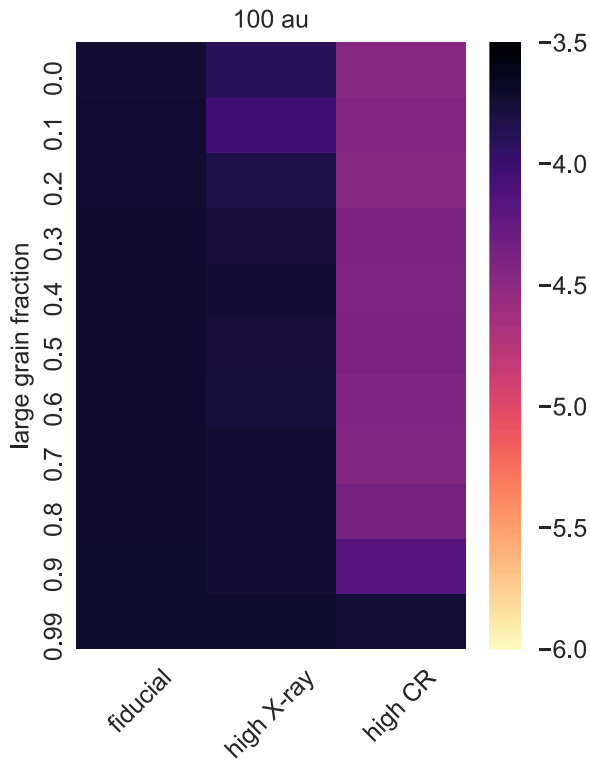


Figure 10. CO abundance relative to the initial abundance of 10^{-4} at 100 au for models with a reduced water/oxygen abundance.

Reaction rates for grain surface chemistry involving more complex species are not currently well constrained, particularly for reactions involving CH_3OH (Cuppen et al. 2017). Inclusion of these reactions in our network would be premature.

3.4. Reduced Oxygen Abundance

CO is able to be reprocessed into CO_2 because of the presence of water. However, observations suggest that the outer disks of many systems are depleted in water vapor (Du et al. 2015, 2017). Additionally, Bergin et al. (2016) find that the rings of hydrocarbon emission observed in TW Hya and DM Tau are best reproduced by models where $\text{C}/\text{O} > 1$ in the gas. To explore how a water and oxygen poor environment affects the volatile carbon chemistry, we remove the initial water ice abundance and rerun the $0.03 M_\odot$ fiducial, hiCR, and hiXR models. The resulting CO abundances are shown in Figures 10 and 11. Of the 33 models water poor models, after 1 Myr 30.3% are depleted in CO in the inner disk and 33.3% are depleted in the outer disk. By 6 Myr this has risen to 57.6% for the inner disk and 45.5% for the outer disk. In comparison, for the corresponding models with a normal water abundance, 42.4% are depleted in the inner disk by 1 Myr, increasing to 69.7% by 6 Myr, while in the outer disk all 33 models are depleted in CO by 1 Myr. Without H_2O providing OH to convert CO into CO_2 , it is much more difficult to remove carbon from CO. Unlike CO_2 formation, the CH_3OH formation pathway is not impeded by the lack of available oxygen. Some CO depletion is still able to take place, though on longer timescales than in the water rich models.

In summary, CO is chemically depleted in the outer disk warm molecular layer when the temperature is low enough for CO_2 to freeze out or there is a high cosmic-ray rate. Additionally, more large grains lead to a more settled disk,

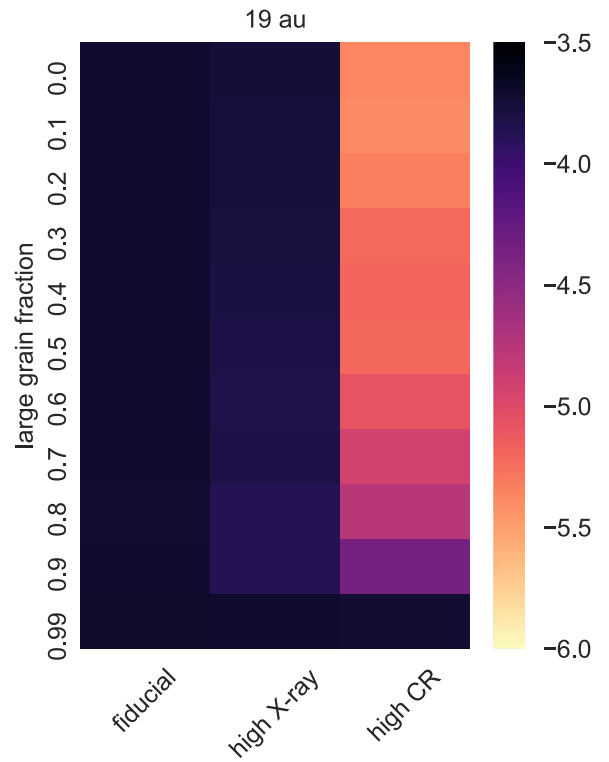


Figure 11. CO abundance relative to the initial abundance of 10^{-4} at 19 au for models with a reduced water/oxygen abundance.

resulting in higher temperatures and a higher UV flux in the warm molecular layer, which impede CO reprocessing. In the inner disk, CO is chemically depleted when there is a high cosmic-ray rate. Throughout the disk, reducing the amount of oxygen available results in less reprocessing of CO.

4. Discussion

Our models show that for an incident cosmic-ray rate of $\sim 10^{-17} \text{ s}^{-1}$ CO is consistently destroyed and carbon is placed into ices, most commonly CO_2 and CH_3OH , and in some cases also CH_4 , in agreement with previous studies (Eistrup et al. 2016; Yu et al. 2016). Reducing the ionization in the models impedes the reprocessing of CO. The modulation of cosmic-rays by the solar wind as well as an inferred low cosmic-ray ionization rate in TW Hya suggest that low cosmic-ray rates due to modulation via winds should be common in disks (Cleeves et al. 2014).

However, in the outer disk, warm molecular layer gas phase CO is reduced by an order of magnitude for the majority of our models, even those without a high cosmic-ray rate. Furthermore, in our fiducial, low ionization models, it is possible to reduce the CO abundance in the inner disk under certain circumstances. In particular, the disk must either have a low overall density, such as in our $0.003 M_\odot$ disk models, or the disk must be settled, with nearly all of the dust mass concentrated in the midplane. Under these circumstances, X-ray ionization or UV photodesorption can drive CO reprocessing. The timescales for such reprocessing are typically longer than in the case of the cosmic-ray-driven chemistry, though order of magnitude depletion can occur on megayear timescales given sufficient dust growth.

Recent high resolution continuum observations of young (< 1 Myr) disks have revealed ringed dust features, which may be indicative of grain growth (ALMA Partnership et al. 2015; Zhang et al. 2015; Pinte et al. 2016). Thus it is possible that disks

are already highly settled by 1 Myr, allowing chemical depletion of CO to occur even without the presence of cosmic-rays. Furthermore, there are many mechanisms, such as accretion onto the central star, photoevaporation, and winds, which will, over time, reduce the density of the disk. Thus, disks for which chemical reprocessing is unable to occur at early times may still experience significant reprocessing at later times.

There are a wide range of physical conditions that permit CO to be chemically reprocessed. After 1 Myr, 99 out of 165 models have a CO abundance less than 10^{-4} at 100 au. This is sufficient to explain the CO abundances of the order of 10^{-5} in many systems (McClure et al. 2016; Long et al. 2017; Miotello et al. 2017). However, the measured CO abundance in TW Hya is 10^{-6} , even interior to the midplane CO snowline (Schwarz et al. 2016; Zhang et al. 2017). A high, ISM level, cosmic-ray rate could result in the large depletion observed, at least in the inner disk, but is inconsistent with the ionization rate derived for this system (Cleeves et al. 2014). Low gas-to-dust ratios based on CO observations in Lupus and Chamaeleon may indicate a two order of magnitude reduction of CO in other systems as well (Long et al. 2017; Miotello et al. 2017). Additional mechanisms beyond chemical reprocessing are needed to explain these observed CO abundances.

CO to dust mass ratios below 100 may be the result of rapid gas loss, though the HD derived mass measurement for TW Hya suggests that this is not the case in at least one system. Vertical mixing can preferentially place CO onto dust grains as ice, with the amount of freeze out dependent on the level of turbulence (Xu et al. 2017). Once on these grains, it can be quickly reprocessed into less volatile species via grain surface reactions. Alternatively, if the small grains grow quickly, they will settle to the midplane, trapping some of the carbon-bearing ices in the interior of large grains (Krijt et al. 2016).

It is important to note that the chemistry explored in this work is for a static disk model, with no mixing between vertical or radial zones. In reality, during the timescales over which CO is being reprocessed, grains are likely to grow, changing the physical conditions at a given location in the disk. Furthermore, the inward drift of grains will transport ices to smaller radii, where they can sublimate. Radial dust drift will also expose the outer disk to higher temperatures and a higher photon flux, similar to the conditions in our warm models with 99% of the dust mass in large grains. In the outer disk, the typical timescale for CO reprocessing is less than 1 Myr. If the timescales for dust growth and drift are longer than those for CO reprocessing, there should still be substantial CO depletion in the outer disk, with carbon-bearing ices trapped in the interior of large grains and/or transported to the inner disk. If, however, reprocessing timescales are longer than those for dust growth and drift, the warmer temperatures will prevent substantial reprocessing of CO. Radial drift of large dust grains is expected to occur within a few hundred orbits (Birnstiel et al. 2016). At 100 au around a $0.8 M_{\odot}$ star, such as that used in our models, one orbit takes approximately 10^3 years, which puts the drift timescale at several 10^5 years, shorter than the typical CO reprocessing time in our models. However, for the majority of the fiducial, hiXR, and hiCR models, half of the initial CO has been reprocessed by 0.1 Myr. Thus, chemical processing of CO in the outer disk should occur so long as the primary source of heating is the central star.

If disks observed to have a reduced CO gas abundance carry their carbon in CO₂ and CH₃OH ice, observations of these

systems should show higher abundances of CO₂ and CH₃OH as the CO abundance decreases. In the inner few astronomical units of a disk, temperatures are warm enough for CO₂ to sublimate from grain surface ices. However, current observations of CO₂ emission at 15 μm are best matched by models with CO₂ abundances in the range 10^{-9} – 10^{-7} (Bosman et al. 2017), well below the typical CO₂ ice abundance in our CO depleted models. This may imply that not all of the CO₂ ice has sublimated, perhaps because grain growth has trapped the ice in the interior of large planetesimals. Alternatively, there could be additional chemical processing of CO₂ ice beyond that currently considered by chemical networks. The *James Webb Space Telescope* will provide crucial insight into this problem by increasing the number of observations of CO₂ in disks. It will also provide additional information regarding the presence of methanol and other hydrocarbons, which may shed light on the issue of carbon evolution.

5. Summary

We have run a grid of 198 chemical models, varying the disk mass, disk temperature, X-ray luminosity, cosmic-ray ionization rate, grain size distribution, and initial water abundance in order to explore the conditions under which gas phase CO can be destroyed in protoplanetary disks.

1. At 100 au, a majority of models (99 out of 165) with ISM-like initial water abundances are depleted, with a CO abundance relative to H₂ less than 10^{-4} after 1 Myr. Of these, only a minority of models (3) are extremely depleted with an abundance of less than 10^{-5} . The requirement for extreme depletion at this radius is the presence of cosmic-rays. If cosmic-rays are not present over a million years of evolution, it is difficult to significantly deplete CO. However, in most cases, after 6 Myr of evolution, significant reductions in the CO abundance can occur.
2. At 19 au, 21 out of 165 models show extreme depletion in CO after 1 Myr. This extreme depletion only occurs in the presence of a high cosmic-ray rate. After 6 Myr of evolution, 45 models are extremely depleted, while 77 models retain over half their initial CO.
3. Based on solar interactions with cosmic-rays, it is possible that cosmic-rays are not abundant in young disk systems (e.g., Cleeves et al. 2013). Thus, it is difficult for chemistry alone to produce the significant reductions in the warm molecular layer CO abundances needed to match current observational constraints. The one exception is low mass ($0.003 M_{\odot}$) disks, for which X-rays can provide the ionization needed to reprocess CO, though on timescales larger than the typical disk lifetime.
4. Removing water from the disk prior to CO depletion hampers the chemical reprocessing of CO.

Therefore, we conclude that chemistry alone is not responsible for the majority of CO depletion seen in disk systems. Other processes must be involved. Viscous mixing could be sending CO to deeper layers of the disk, where it is able to freeze onto grains, which then grow. Additionally, carbon in the form of either CO or CO₂ ice could be locked inside large, many kilometer sized bodies, which are not easily evaporated within 1 Myr. In a subsequent work, we will explore the evolution of CO in the midplane, where conditions differ from those in the warm molecular layer.

This work was supported by funding from NSF grants AST-1514670 and AST-1344133 (INSPIRE) as well as NASA NNX16AB48G. L.I.C. acknowledges the support of NASA through Hubble Fellowship grant HST-HF2-51356.001. K.Z. acknowledges the support of NASA through Hubble Fellowship grant HST-HF2-51401.001-A awarded by the Space Telescope Science Institute, which is operated by the Association of Universities for Research in Astronomy, Inc., for NASA, under contract NAS5-26555.

Appendix A
Additional Figures

The figures in the main text focus primarily on the $0.03 M_{\odot}$ models. In Figures 12–17 we show the corresponding temperature, UV, and X-ray profiles for the 0.003 and $0.1 M_{\odot}$ models. Figure 18 provides an illustrative example of how we define the warm molecular layer for the purpose of our analysis.

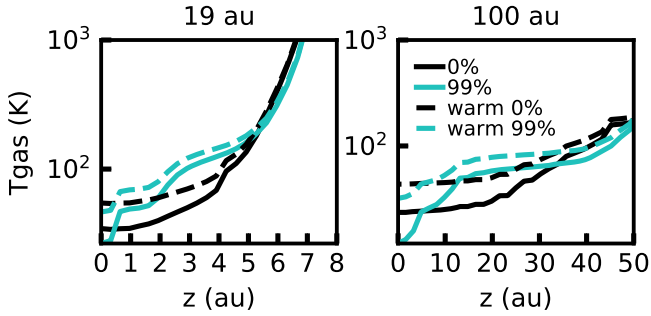


Figure 12. Vertical gas temperature profiles at 19 and 100 au for the $0.003 M_{\odot}$ disk. The 0% large grain model is shown in black and the 99% large grain model is shown in teal. Dashed lines indicate the temperature in the warm disk models.

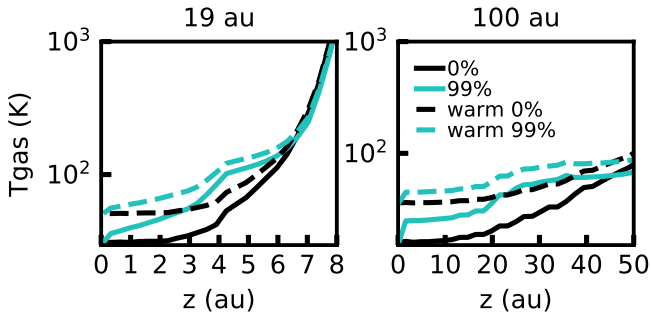


Figure 13. Vertical gas temperature profiles at 19 and 100 au for the $0.1 M_{\odot}$ disk. The 0% large grain model is shown in black and the 99% large grain model is shown in teal. Dashed lines indicate the temperature in the warm disk models.

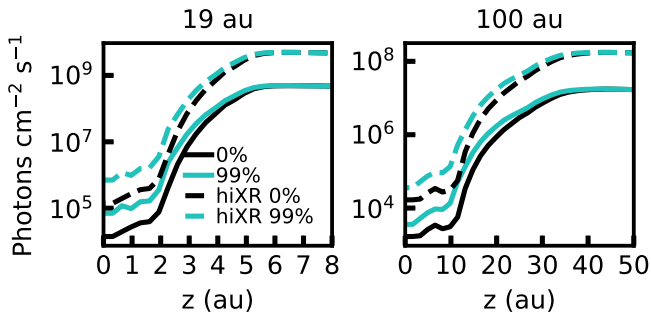


Figure 14. Vertical profiles of the integrated X-ray flux at 19 and 100 au for the $0.003 M_{\odot}$ disk. The 0% large grain model is shown in black and the 99% large grain model is shown in teal. Dashed lines indicate the temperature in the warm disk models.

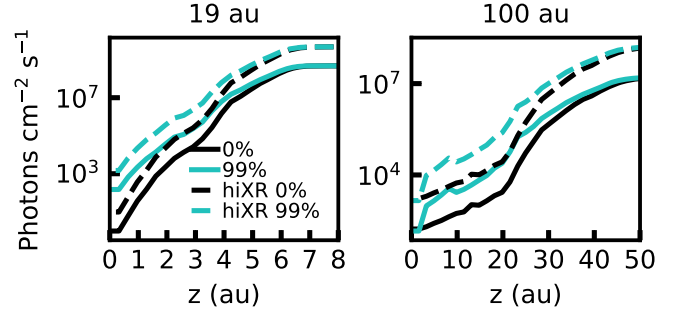


Figure 15. Vertical profiles of the integrated X-ray flux at 19 and 100 au for the $0.1 M_{\odot}$ disk. The 0% large grain model is shown in black and the 99% large grain model is shown in teal. Dashed lines indicate the temperature in the warm disk models.

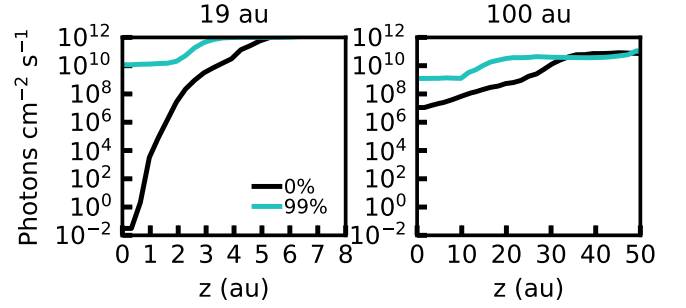


Figure 16. Vertical profiles of the integrated UV flux at 19 and 100 au for the $0.003 M_{\odot}$ disk. The 0% large grain model is shown in black and the 99% large grain model is shown in teal. Dashed lines indicate the temperature in the warm disk models.

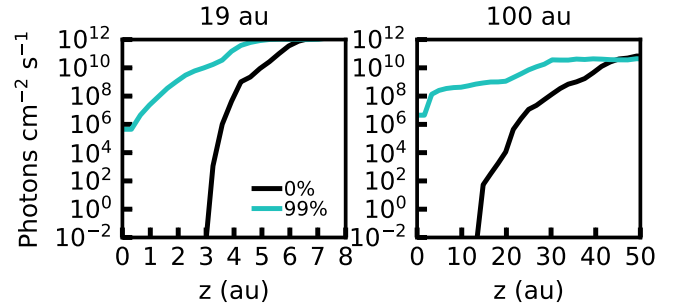


Figure 17. Vertical profiles of the integrated UV flux at 19 and 100 au for the $0.1 M_{\odot}$ disk. The 0% large grain model is shown in black and the 99% large grain model is shown in teal. Dashed lines indicate the temperature in the warm disk models.

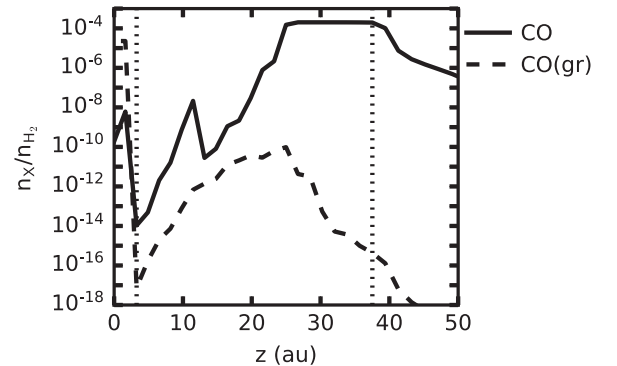


Figure 18. CO gas and ice abundance as a function of height in the disk at 100 au for the fiducial $0.03 M_{\odot}$ model with 80% large grains. The vertical dotted lines indicate the boundaries of the warm molecular layer.

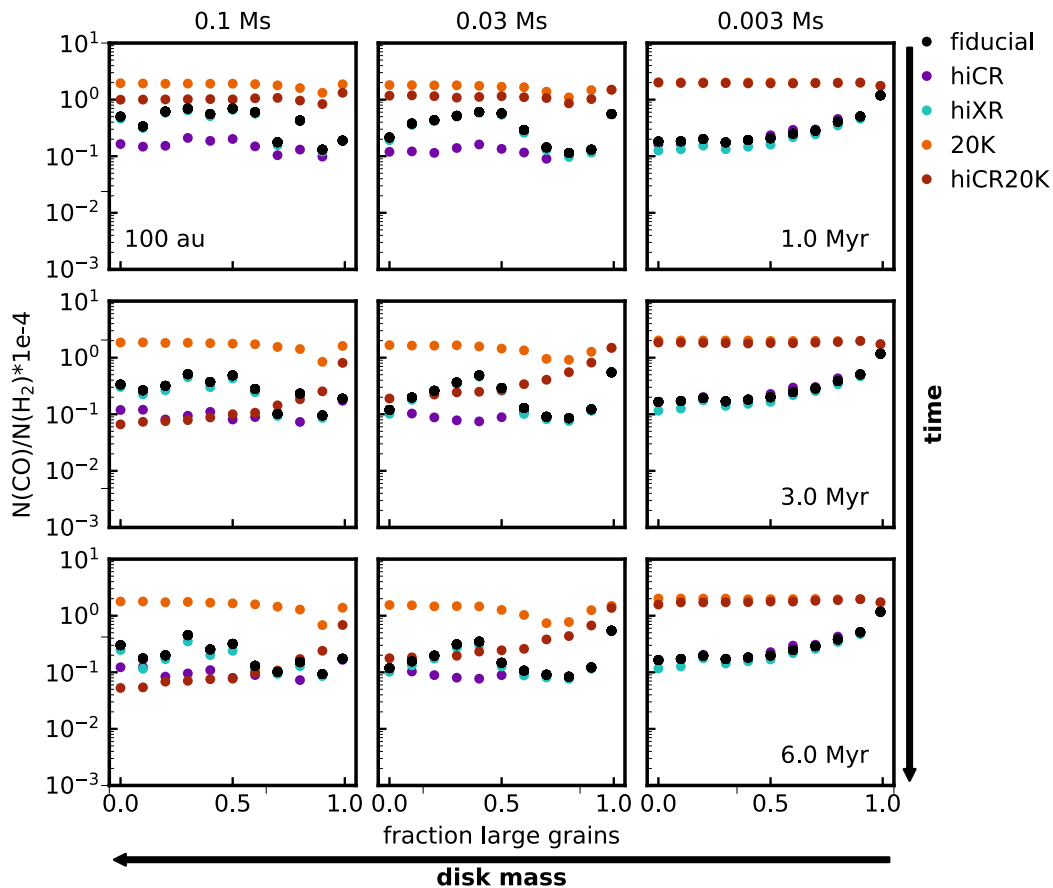


Figure 19. Predicted gas phase CO abundance in the warm molecular layer at 100 au for each model.

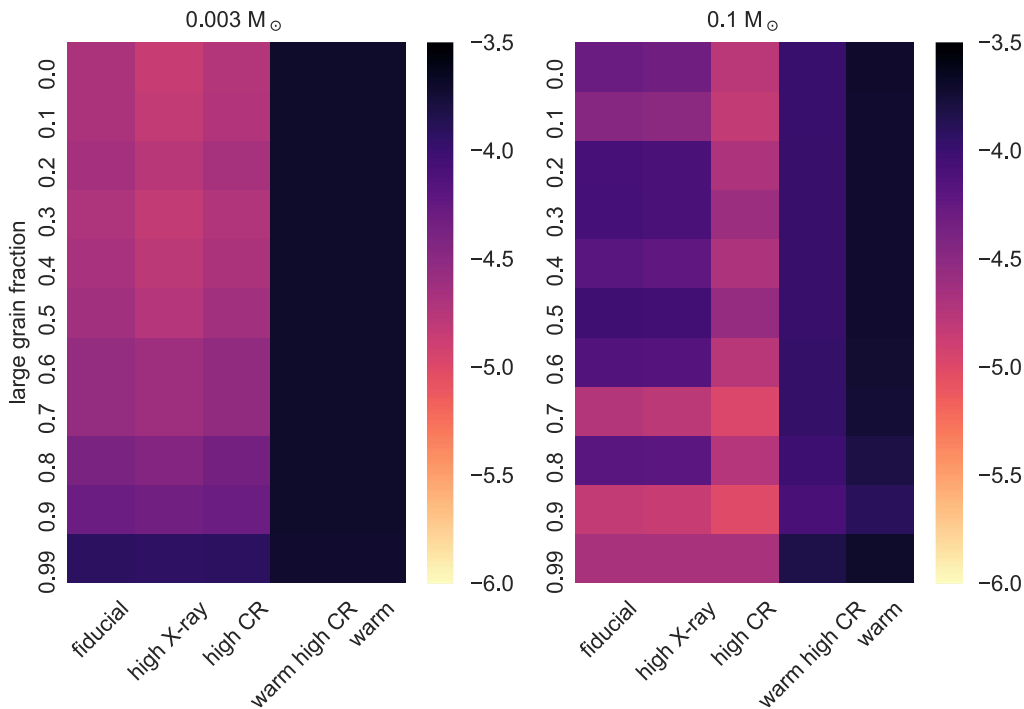


Figure 20. Log CO abundance relative to H_2 at 100 au for each model with disk masses of 0.003 and $0.1 M_{\odot}$.

Figures 19–25 provide further information on how the CO abundance evolves under different conditions. Figure 19 summarizes how the CO abundance in the warm molecular

layer at 100 au changes depending on the ionization and temperature structure, fraction of large grains, disk mass, and time. Figure 20 shows the CO abundances in the 0.003 and

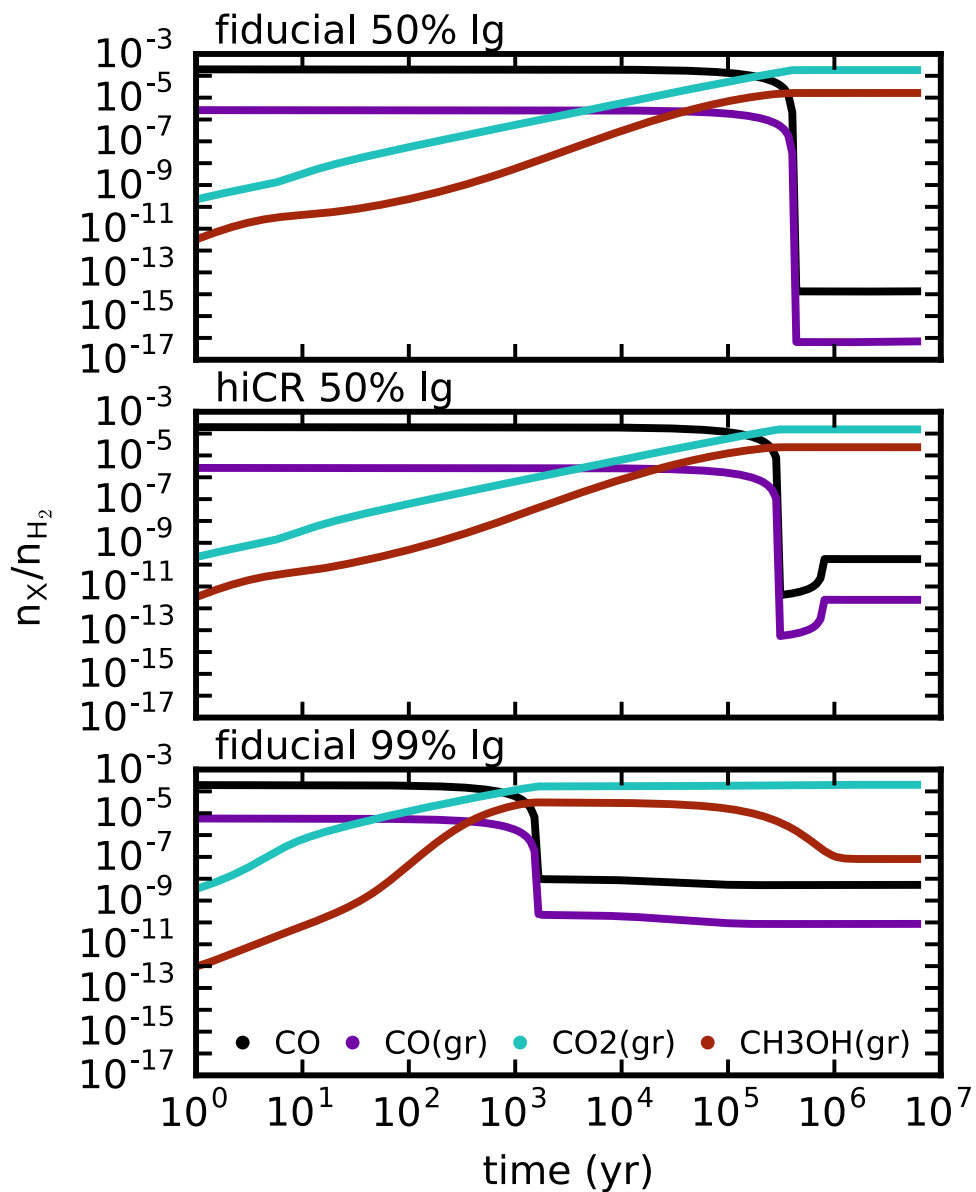


Figure 21. Abundances of the most abundant carbon species as a function of time for select $0.03 M_{\odot}$ models at 100 au in radius and for a height of 11.5 au.

$0.01 M_{\odot}$ disks corresponding to those for the $0.03 M_{\odot}$ disks in Figure 6. Figure 21 follows the abundance of the dominant carbon bearing molecules as a function of time for a single point in the disk for three different models. In the outer disk

increasing the fraction of large grains allows CO reprocessing to occur sooner but to a lesser extent.

The CO abundances in the inner disk are summarized in Figures 22–23, while Figure 24 illustrates how the build-up of

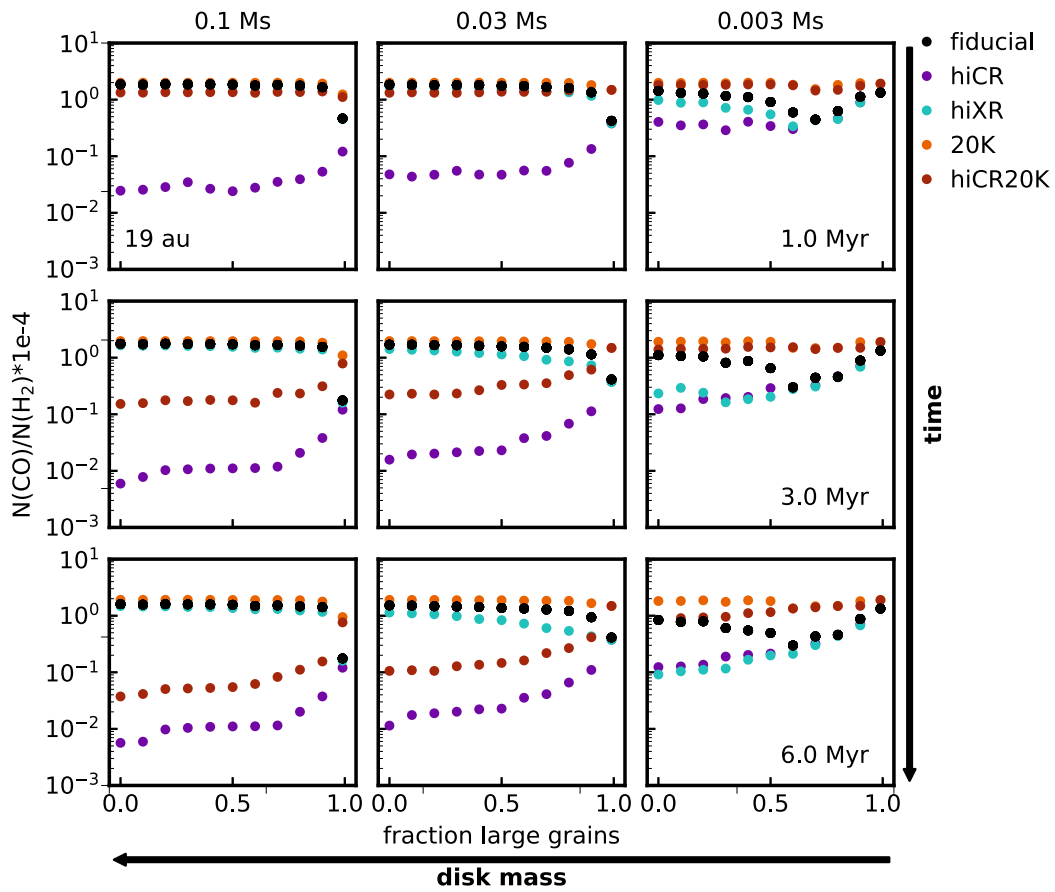


Figure 22. Predicted gas phase CO abundance in the warm molecular layer at 19 au for each model.

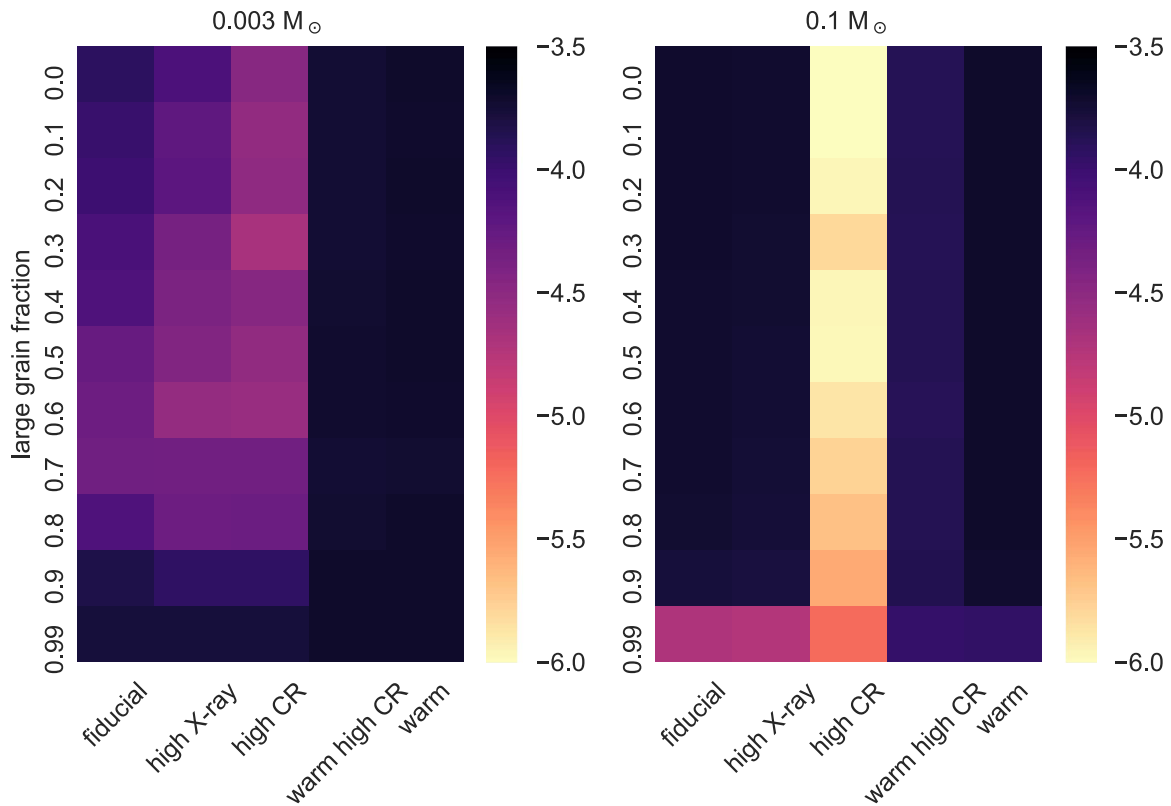


Figure 23. Log CO abundance relative to H_2 at 19 au for each model with disk masses of 0.003 and 0.1 M_\odot .

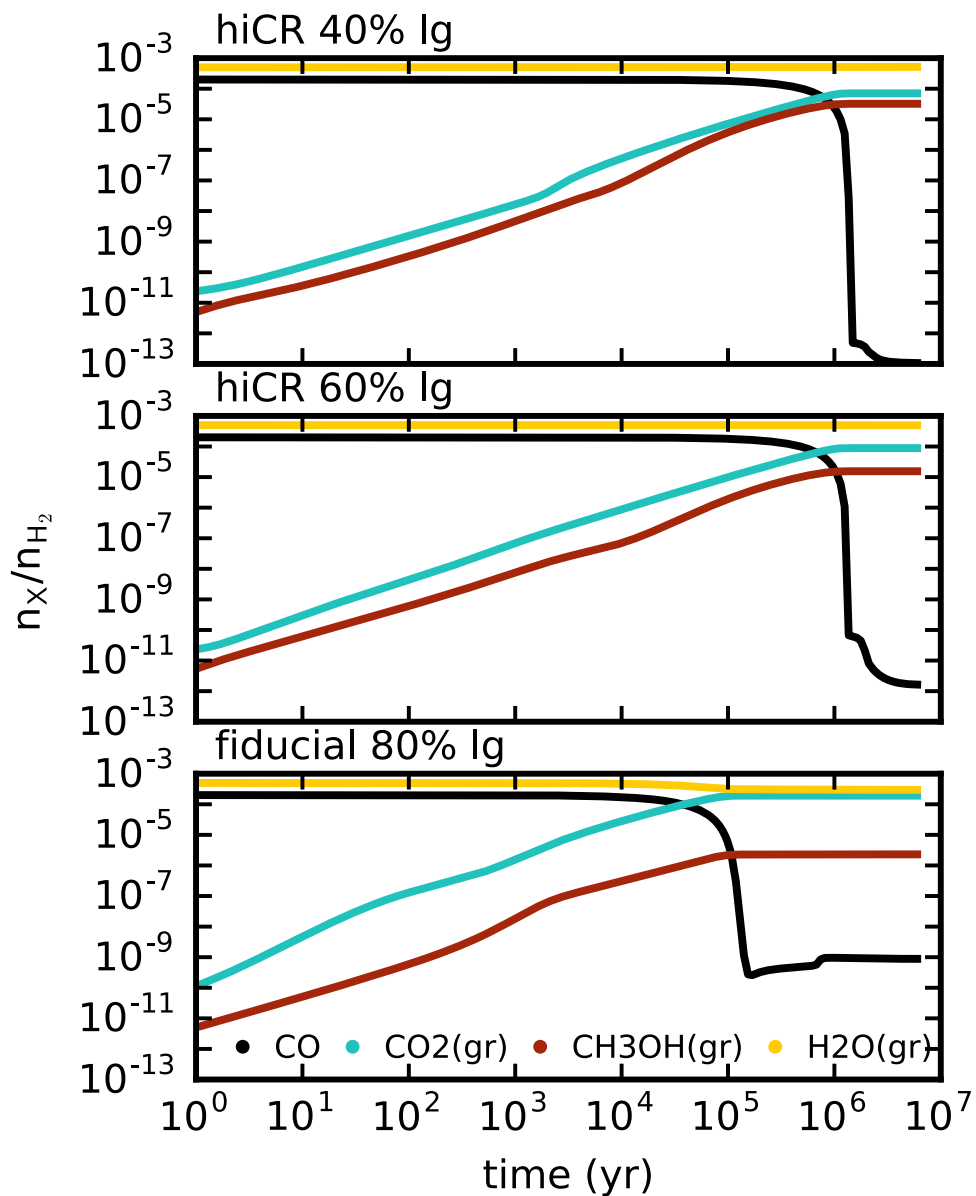


Figure 24. Abundances as a function of time for select hiCR $0.03 M_{\odot}$ models at a radius of 19 au and a height of 2.3 au.

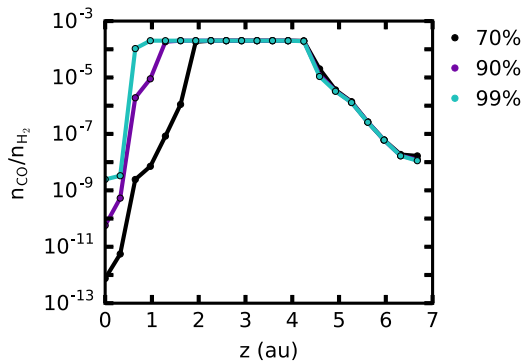


Figure 25. CO abundance as a function of height in the disk at 19 au for the fiducial $0.003 M_{\odot}$ models with different large grain fractions.

carbon bearing ices in the inner disk depends on both the cosmic-ray ionization rate and the fraction of large grains. Finally, Figure 25 shows how less CO is reprocessed as the fraction of large grains increases.

Appendix B Abundance Tables

Tables 4–5 list the top five most abundance carbon bearing species in the warm molecular layer for each model after 1 Myr in the outer and inner disk respectively. For every model in which CO has been significantly reprocessed the dominate carbon bearing species is either CO_2 ice or CH_3OH ice. Additional carbon bearing ices formed as a consequence of CO reprocessing include HCN and CH_4 .

Table 4
Top Five Most Abundant Carbon Bearing Species in the Warm Molecular Layer at 100 au for Each Model after 1 Myr

Model	M_{disk}	f_l	Species	Abundance	Species	Abundance	Species	Abundance	Species	Abundance	Species	Abundance
fiducial	0.003	0.0	CO ₂ (gr)	1.75e-04	CO	2.04e-05	CH ₃ OH(gr)	4.37e-06	CN(gr)	7.93e-07	OCN(gr)	4.18e-07
fiducial	0.003	0.1	CO ₂ (gr)	1.73e-04	CO	2.06e-05	CH ₃ OH(gr)	5.98e-06	CN(gr)	7.32e-07	OCN(gr)	5.03e-07
fiducial	0.003	0.2	CO ₂ (gr)	1.70e-04	CO	2.25e-05	CH ₃ OH(gr)	7.35e-06	CN(gr)	6.35e-07	OCN(gr)	5.74e-07
fiducial	0.003	0.3	CO ₂ (gr)	1.73e-04	CO	1.97e-05	CH ₃ OH(gr)	6.93e-06	OCN(gr)	6.53e-07	CN(gr)	5.70e-07
fiducial	0.003	0.4	CO ₂ (gr)	1.74e-04	CO	2.17e-05	CH ₃ OH(gr)	4.41e-06	OCN(gr)	7.03e-07	CN(gr)	4.60e-07
fiducial	0.003	0.5	CO ₂ (gr)	1.75e-04	CO	2.33e-05	CH ₃ OH(gr)	2.21e-06	OCN(gr)	7.99e-07	CH ₄ (gr)	3.03e-07
fiducial	0.003	0.6	CO ₂ (gr)	1.71e-04	CO	2.81e-05	CH ₃ OH(gr)	8.04e-07	OCN(gr)	7.73e-07	CH ₄ (gr)	3.43e-07
fiducial	0.003	0.7	CO ₂ (gr)	1.72e-04	CO	2.82e-05	OCN(gr)	8.36e-07	CH ₃ OH(gr)	4.80e-07	CH ₄ (gr)	1.50e-07
fiducial	0.003	0.8	CO ₂ (gr)	1.60e-04	CO	4.07e-05	OCN(gr)	7.19e-07	CH ₃ OH(gr)	1.41e-07	C ⁺	1.08e-07
fiducial	0.003	0.9	CO ₂ (gr)	1.50e-04	CO	5.05e-05	OCN(gr)	4.28e-07	CH ₃ OH(gr)	2.22e-07	C ⁺	2.05e-07

Note. Abundances are relative to H₂.

(This table is available in its entirety in machine-readable form.)

Table 5
Top Five Most Abundant Carbon Bearing Species in the Warm Molecular Layer at 19 au for Each Model after 1 Myr

Model	M_{disk}	f_l	Species	Abundance	Species	Abundance	Species	Abundance	Species	Abundance	Species	Abundance
fiducial	0.003	0.0	CO	1.21e-04	CO ₂ (gr)	7.37e-05	CH ₃ OH(gr)	8.96e-07	HCN(gr)	7.52e-07	HNC(gr)	5.73e-07
fiducial	0.003	0.1	CO	1.03e-04	CO ₂ (gr)	9.08e-05	HCN(gr)	8.73e-07	CH ₃ OH(gr)	8.42e-07	HNC(gr)	5.60e-07
fiducial	0.003	0.2	CO	9.81e-05	CO ₂ (gr)	9.65e-05	HCN(gr)	8.42e-07	CH ₃ OH(gr)	6.94e-07	HNC(gr)	5.62e-07
fiducial	0.003	0.3	CO ₂ (gr)	1.14e-04	CO	8.14e-05	CH ₃ OH(gr)	8.35e-07	HCN(gr)	7.54e-07	HNC(gr)	5.80e-07
fiducial	0.003	0.4	CO ₂ (gr)	1.20e-04	CO	7.49e-05	HCN(gr)	1.38e-06	CH ₃ OH(gr)	8.77e-07	HNC(gr)	5.85e-07
fiducial	0.003	0.5	CO ₂ (gr)	1.42e-04	CO	5.38e-05	HCN(gr)	9.24e-07	CH ₃ OH(gr)	6.30e-07	HNC(gr)	4.83e-07
fiducial	0.003	0.6	CO ₂ (gr)	1.48e-04	CO	4.96e-05	CH ₃ OH(gr)	1.88e-06	HCN(gr)	7.54e-07	HNC(gr)	3.60e-07
fiducial	0.003	0.7	CO ₂ (gr)	1.52e-04	CO	4.72e-05	CH ₃ OH(gr)	1.15e-06	HCN(gr)	6.60e-07	HNC(gr)	2.48e-07
fiducial	0.003	0.8	CO ₂ (gr)	1.26e-04	CO	7.55e-05	CH ₃ OH(gr)	1.68e-07	HCN(gr)	1.33e-07	OCN(gr)	4.12e-08
fiducial	0.003	0.9	CO	1.48e-04	CO ₂ (gr)	5.34e-05	CH ₃ OH(gr)	9.93e-08	OCN(gr)	1.93e-08	HCN(gr)	1.36e-08

Note. Abundances are relative to H₂.

(This table is available in its entirety in machine-readable form.)

ORCID iDs

Kamber R. Schwarz  <https://orcid.org/0000-0002-6429-9457>
 Edwin A. Bergin  <https://orcid.org/0000-0003-4179-6394>
 Karin I. Öberg  <https://orcid.org/0000-0001-8798-1347>
 Geoffrey A. Blake  <https://orcid.org/0000-0003-0787-1610>

References

- Aikawa, Y., & Herbst, E. 1999, *A&A*, **351**, 233
 ALMA Partnership, Brogan, C. L., Pérez, L. M., et al. 2015, *ApJL*, **808**, L3
 Ansdell, M., Williams, J. P., van der Marel, N., et al. 2016, *ApJ*, **828**, 46
 Bai, X.-N. 2016, *ApJ*, **821**, 80
 Bergin, E. A., Cleeves, L. I., Crockett, N., & Blake, G. A. 2014, *FaDi*, **168**, 61
 Bergin, E. A., Cleeves, L. I., Gorti, U., et al. 2013, *Natur*, **493**, 644
 Bergin, E. A., Du, F., Cleeves, L. I., et al. 2016, *ApJ*, **831**, 101
 Bergin, E. A., & Williams, J. P. 2017, in *Astrophysics and Space Science Library*, Vol. 445, Formation, Evolution, and Dynamics of Young Solar Systems, ed. M. Pessah & O. Gressel (Berlin: Springer), 1
 Bethell, T. J., & Bergin, E. A. 2011a, *ApJ*, **740**, 7
 Bethell, T. J., & Bergin, E. A. 2011b, *ApJ*, **739**, 78
 Birnstiel, T., Fang, M., & Johansen, A. 2016, *SSRv*, **205**, 41
 Bosman, A. D., Bruderer, S., & van Dishoeck, E. F. 2017, *A&A*, **601**, A36
 Brickhouse, N. S., Cranmer, S. R., Dupree, A. K., Luna, G. J. M., & Wolk, S. 2010, *ApJ*, **710**, 1835
 Cleeves, L. I., Adams, F. C., & Bergin, E. A. 2013, *ApJ*, **772**, 5
 Cleeves, L. I., Bergin, E. A., Alexander, C. M. O., et al. 2014, *Sci*, **345**, 1590
 Cleeves, L. I., Bergin, E. A., Qi, C., Adams, F. C., & Öberg, K. I. 2015, *ApJ*, **799**, 204
 Cuppen, H. M., Walsh, C., Lamberts, T., et al. 2017, *SSRv*, **212**, 1
 Draine, B. T., & Lee, H. M. 1984, *ApJ*, **285**, 89
 Du, F., Bergin, E. A., Hogerheijde, M., et al. 2017, *ApJ*, **842**, 98
 Du, F., Bergin, E. A., & Hogerheijde, M. R. 2015, *ApJL*, **807**, L32
 Dutrey, A., Guilloteau, S., & Simon, M. 1994, *A&A*, **286**, 149
 Eistrup, C., Walsh, C., & van Dishoeck, E. F. 2016, *A&A*, **595**, A83
 Favre, C., Cleeves, L. I., Bergin, E. A., Qi, C., & Blake, G. A. 2013, *ApJL*, **776**, L38
 Fogel, J. K. J., Bethell, T. J., Bergin, E. A., Calvet, N., & Semenov, D. 2011, *ApJ*, **726**, 29
 Gleeson, L. J., & Axford, W. I. 1968, *ApJ*, **154**, 1011
 Harries, T. J. 2000, *MNRAS*, **315**, 722
 Kama, M., Bruderer, S., Carney, M., et al. 2016, *A&A*, **588**, A108
 Kastner, J. H., Huenemoerder, D. P., Schulz, N. S., & Weintraub, D. A. 1999, *ApJ*, **525**, 837
 Krijt, S., & Ciesla, F. J. 2016, *ApJ*, **822**, 111
 Krijt, S., Ciesla, F. J., & Bergin, E. A. 2016, *ApJ*, **833**, 285
 Long, F., Herczeg, G. J., Pascucci, I., et al. 2017, *ApJ*, **844**, 99
 Mathis, J. S., Rumpl, W., & Nordsieck, K. H. 1977, *ApJ*, **217**, 425
 McClure, M. K., Bergin, E. A., Cleeves, L. I., et al. 2016, *ApJ*, **831**, 167
 McElroy, D., Walsh, C., Markwick, A. J., et al. 2013, *A&A*, **550**, A36
 Miotello, A., Bruderer, S., & van Dishoeck, E. F. 2014, *A&A*, **572**, A96
 Miotello, A., van Dishoeck, E. F., Williams, J. P., et al. 2017, *A&A*, **599**, A113
 Pinte, C., Dent, W. R. F., Ménard, F., et al. 2016, *ApJ*, **816**, 25
 Raassen, A. J. J. 2009, *A&A*, **505**, 755
 Reboussin, L., Wakelam, V., Guilloteau, S., Hersant, F., & Dutrey, A. 2015, *A&A*, **579**, A82
 Salyk, C., Pontoppidan, K. M., Blake, G. A., et al. 2008, *ApJL*, **676**, L49
 Schwarz, K. R., Bergin, E. A., Cleeves, L. I., et al. 2016, *ApJ*, **823**, 91
 Smith, I. W. M., Herbst, E., & Chang, Q. 2004, *MNRAS*, **350**, 323
 Webber, W. R. 1998, *ApJ*, **506**, 329
 Williams, J. P., & Best, W. M. J. 2014, *ApJ*, **788**, 59
 Xu, R., Bai, X.-N., & Öberg, K. 2017, *ApJ*, **835**, 162
 Youdin, A. N., & Lithwick, Y. 2007, *Icar*, **192**, 588
 Yu, M., Willacy, K., Dodson-Robinson, S. E., Turner, N. J., & Evans, N. J., II 2016, *ApJ*, **822**, 53
 Zhang, K., Bergin, E. A., Blake, G. A., Cleeves, L. I., & Schwarz, K. R. 2017, *NatAs*, **1**, 0130
 Zhang, K., Blake, G. A., & Bergin, E. A. 2015, *ApJL*, **806**, L7